Ultrasonics 93 (2019) 18–25

Contents lists available at ScienceDirect

Ultrasonics

journal homepage: www.elsevier.com/locate/ultras

Acoustic manipulation of particles in a cylindrical cavity: Theoretical and experimental study on the effects of boundary conditions

Di Xu[a], Feiyan Cai[a,*], Mian Chen[a], Fei Li[a], Chen Wang[a], Long Meng[a], Dehui Xu[b], Wei Wang[c], Junru Wu[d], Hairong Zheng[a]

[a] Paul C. Lauterbur Research Center for Biomedical Imaging, Institute of Biomedical and Health Engineering, Shenzhen Institutes of Advanced Technology, Chinese Academy of Sciences, Shenzhen 518055, People's Republic of China
[b] Science and Technology on Micro-system Laboratory, Shanghai Institute of Microsystem and Information Technology, Chinese Academy of Science, 865 Changning Road, Shanghai 200050, People's Republic of China
[c] School of Materials Science and Engineering, Harbin Institute of Technology, Shenzhen Graduate School, Shenzhen 518055, People's Republic of China
[d] Department of Physics, University of Vermont, Burlington, VT 05405, USA

ARTICLE INFO

Keywords:
Standing wave
Acoustic manipulation
Cylindrical cavity
Acoustic radiation force
Boundary condition

ABSTRACT

Precise manipulation of microparticles in microchannels is a primary technique for numerous lab-on-a-chip bioengineering research and applications, as it determines the chip's functions and analytical results. Acoustic manipulation, using the acoustic radiation force, is a compact, versatile and contactless manipulation technique, which can be easily integrated with other microfluidic components. It is our main purpose to report the effect of boundary condition of a cylindrical microfluidic cavity on the acoustic particles' manipulation. A device consisting of a cylindrical cavity in a silicon wafer with three kinds of top boundary conditions (rigid, soft, and imperfect rigid boundary) has been built. The corresponding distributions of acoustic radiation force are analyzed analytically and numerically. Experiments are performed with 2.5 μm radius polystyrene microspheres in the cavity covered by three reflective layers (340 μm-thick glass, 400 μm-thick PDMS, and 660 μm-thick glass film), respectively, which specify the three different boundary conditions at the top of the cavity. It is demonstrated that the boundary condition of a cavity influences the acoustic radiation force and the stable positions of particles, and this is in agreement with the theoretical predictions. Thus, the effects of boundary conditions need to be considered for precise acoustic manipulation.

1. Introduction

The ability to perform precise and dexterous manipulation of micro-sized particles in a microchannel is invaluable for many applications in biology, chemistry, engineering and physics [1–16]. Manipulation of particles by ultrasonic waves has been extensively studied since the early 1900s. The basic principle of this technique involves the particles in the acoustic field experiencing an acoustic radiation force (ARF) via absorption and reflection. Compared to other manipulation technologies, such as magnetic or optical tweezers, and dielectrophoresis, ultrasonic manipulation has shown its advantages as being versatile, inexpensive, and easily integrated with other microfluidic components. In microfluidic applications, the ultrasonic standing wave is typically used. Many works have been reported on the study of particles in a standing field, including the fabrication of microfluidic channels for standing field generation [9–11], theoretical calculations [17–19] and experimental observations of the ARFs in the standing field for trapping, moving, and sorting microparticles [15,20,21], cells and active organisms [1–8].

An efficient device that generates an acoustic standing wave is to excite harmonic resonance modes in a fluid-filled cavity or channel. It commonly has a simple one-dimensional (1D) linear channel or two-dimensional (2D) rectangular channel structure combined with lead zirconate titanate (PZT) or interdigital transducer (IDT) sources to generate a bulk standing wave in a channel or a surface standing wave on the surface of the channel. When the channel wall is considered as a rigid boundary, by adjusting the driving wavelength to match the width or height of the microfluidic channel, generally, $l\lambda = 2L$ ($l = 1, 2. ..$ represents the mode of the vibration inside the channel, L is the dimension of the channel), 1D or 2D standing waves can be generated in the microfluidic channel, and thus particles can be trapped on the pressure node or antinode depending on the compressibility and density

* Corresponding author.
E-mail addresses: fy.cai@siat.ac.cn (F. Cai), hr.zheng@siat.ac.cn (H. Zheng).

https://doi.org/10.1016/j.ultras.2018.10.003
Received 12 December 2017; Received in revised form 8 October 2018; Accepted 8 October 2018
Available online 09 October 2018
0041-624X/

of the particles compared with those of the ambient fluid. By modulating the relative phase of the sources or slightly tuning the driving frequency, the pressure node can be moved, thus inducing particle motion accordingly [6,7].

Besides 1D linear or 2D rectangular channels, a cylindrical cavity can also be used to generate a standing wave in the axial and radial directions. For example, Kaduchak et al. constructed a hollow, cylindrical piezoelectric tube driven at the Bessel resonance mode in the radial direction to levitate and concentrate drops of water in air [9]. Yamahira et al. built a cylindrical vessel fixed on a stainless steel plate with the transducer excited at the bottom to investigate the translation and rotation of polystyrene (PS) fibers in the axial direction, while in the radial direction no standing wave existed because the radius of the cylinder did not match the corresponding wavelength [13]. In a similar way, Wang et al. set up a cylindrical vessel by applying polyimide Kapton tape with a height of $L = 0.5\lambda$ while the radial scale was several orders of the wavelength [14]. By using this cylindrical vessel, versatile experimental phenomena were observed at the center plane of the cavity, such as PS particles patterned with rings, streaks and aggregations, metal microrods motion in the axial direction, rotation in plane, chain assembly and pattern formation [14]. These versatile patterns and motion phenomena in the radial plane may be due to the complex ARF distribution in this plane, which may originate from the intricate boundary conditions and multiple modes excited in the cavity.

To comprehend the manipulation phenomena of micro-sized particles in microchannels, in this work, we theoretically and experimentally investigate the effects of boundary conditions on acoustic manipulation of particles in a cylindrical cavity. First, we present the analytical studies on ARF distribution in a cylindrical cavity considering rigid and soft top boundary conditions. Then, the numerical and experimental results of these manipulation phenomena of 2.5 μm radius PS microspheres in a cylindrical cavity with three different kinds of top reflective layers, rigid (340 μm-thick glass), soft (400 μm-thick PDMS) and imperfect rigid (660 μm-thick glass film) boundaries are presented. Finally, we discuss the relationship between the stable manipulation phenomena and the boundary conditions. The experimental results coincide with the theoretical predictions that the stable trapping positions of the particles can be greatly affected by the boundary conditions. We believe this work can provide experimental support for the influence of boundary conditions on acoustic manipulation in a cylindrical cavity.

2. Experiments and theoretical model

2.1. Experimental setup

A schematic view of the experimental setup is shown in Fig. 1. A cylindrical cavity (height $L = 186$ μm, radius $a = 419$ μm) is dry-etched in the surface of a silicon plate (thickness 440 μm). A piezoelectric (PZT) plate as the actuator is mounted on the bottom of the silicon plate. As two driving frequencies are utilized in the experiment, two PZT plates with resonance frequencies of 4 MHz (thickness 540 μm) and 6.28 MHz (thickness 383 μm) are used, respectively. These PZT plates are actuated using continuous sinusoidal electric signals ($< 10\ V_{pp}$) by a signal generator (AFG 3102, Tektronix, Beaverton, OR, USA) without an amplifier. The cavity is filled with a 10 wt% salt solution and polystyrene (PS) microspheres (B1510021, Aladdin Industrial Corp., Shanghai, CN) with a radius of 2.5 μm. Initially, the PS particles are suspended in the liquid as the densities of the liquid and the PS particles are identical [13]. An optical microscope (N14JZBPB03-26, Leica, GER) combined with a camera (optiMOS, QImaging, CA) is positioned directly above the cavity to image the pattern formation of the PS particles [15]. A reflective plate covers the cavity indicating the top boundary. In order to indicate different top boundary conditions, we choose a glass plate with thickness of 340 μm, a polydimethylsiloxane (PDMS) plate with thickness of 400 μm, and a glass plate with thickness of 660 μm to represent rigid, soft and imperfect rigid boundaries, respectively. The acoustic properties of these three plates are investigated in the following section of numerical model.

2.2. Analytical model

Consider a cylindrical cavity of height L and radius a, assuming that the cylindrical wall boundaries and the bottom boundary are perfectly rigid, while the top boundary of the cavity is determined by the property of the reflective plate. The pressure of the eigen mode in this cavity can be written as [22]:

$$p = A_{mnl} J_m(k_{mn} r)\cos(m\phi + \phi_m)\cos(k_{zl} z + \varphi_{zl})e^{i\omega t} \tag{1}$$

The quantum numbers m, n and l, (mnl) represent the normal mode in ϕ, r and z coordinates. A_{mnl} and ϕ_m denote the pressure amplitude and initial phase. Since there are no reflecting boundaries for cylindrical waves, ϕ_m can be considered as an arbitrary phase constant, letting $\phi_m = 0$ in the following calculations. As the rigid boundary condition in the cylindrical wall, the wavenumber k in the radial direction can be written as $k_{mn} = j'_{mn}/a$, where j'_{mn} is the nth extremum of the mth Bessel function of the first kind. k_{zl} and φ_{zl} are determined by the top boundary condition of the cavity. The wavenumber$k$is specified by $k = \omega/c = (k_{mn}^2 + k_{zl}^2)^{1/2}$. In addition, the associated velocity field can be derived from $\boldsymbol{v} = -i\nabla p/(\rho\omega)$ [23].

It is well known that the ARF $\boldsymbol{F}^{rad}$on a small, spherical particle ($r_p \ll \lambda$) in an inviscid fluid is the gradient of an acoustic potential U^{rad} [17,18,24],

$$\boldsymbol{F}^{rad} = -\nabla U^{rad} \tag{2}$$

$$U^{rad} = 2\pi r_p^3 \left(\frac{\langle p^2 \rangle}{3\rho c^2} f_1 - \rho \frac{\langle \boldsymbol{v}^2 \rangle}{2} f_2 \right) \tag{3}$$

where $f_1 = 1 - \frac{\rho c^2}{\rho_p c_p^2}$, $f_2 = \frac{2(\rho_p - \rho)}{2\rho_p + \rho}$, $\langle p^2 \rangle$ and $\langle \boldsymbol{v}^2 \rangle$ are the mean-square fluctuations of the incoming first-order pressure and velocity in the

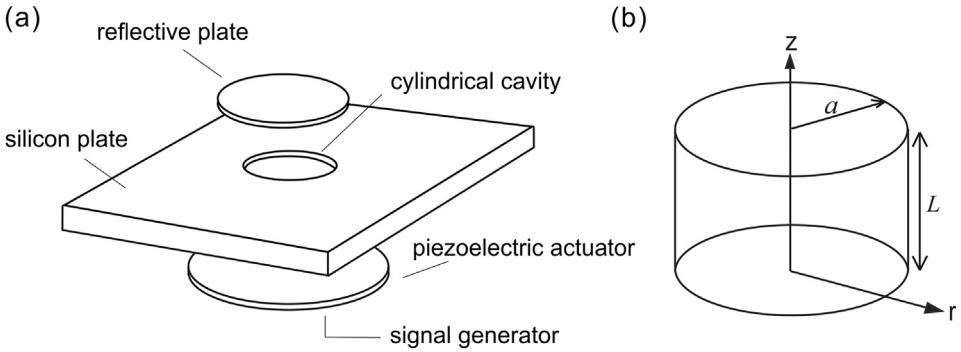

Fig. 1. (a) Schematic view of the experimental setup. (b) Geometry of the cylindrical cavity.

wave at the point where the particle is located. The terms ρ_p and ρ refer to the density, and c_p and c refer to the speed of sound in the particles and fluid, respectively, and r refers to the particle radius. The angle brackets represent time-averaging.

After calculating the mean-square fluctuations of the acoustic pressure and velocity and substituting them into Eq. (3), the dimensionless acoustic potential of the (mnl) mode in this cavity is

$$\bar{U}^{rad} = \frac{f_1}{3}J_m^2(\chi)\cos^2 m\phi\cos^2\zeta - \frac{f_2}{2}\left\{\left(\frac{k_{mn}}{k}\right)^2\left[\left(\frac{mJ_m(\chi)}{\chi}\right)^2\cos^2\zeta - \frac{2mJ_m(\chi)J_{m+1}(\chi)}{\chi}\cos^2 m\phi\cos^2\zeta + J_{m+1}^2(\chi)\cos^2 m\phi\cos^2\zeta\right] + \left(\frac{k_{zl}}{k}\right)^2 J_m^2(\chi)\cos^2 m\phi\sin^2\zeta\right\} \tag{4}$$

where $\chi = k_{mn}r$ and $\zeta = k_{zl}z + \varphi_{zl}$.

Thus, the dimensionless force components of the (mnl) mode in the cylindrical cavity are

$$\bar{F}_r = -\frac{\partial\bar{U}^{rad}}{\partial r} = 2J_m(\chi)k_{mn}\left(\frac{mJ_m(\chi)}{\chi} - J_{m+1}(\chi)\right)\cos^2 m\phi\left(-\frac{f_1}{3}\cos^2\zeta + \frac{f_2}{2}\left(\frac{k_{zl}}{k}\right)^2\sin^2\zeta\right) - \frac{f_2}{2}\left(\frac{k_{mn}}{k}\right)^2\cos^2\zeta\left\{\frac{2m}{r}\left[\frac{(m-1)J_m(\chi)}{\chi} - J_{m+1}(\chi)\right]\left[\frac{mJ_m(\chi)}{\chi} - \cos^2 m\phi J_{m+1}(\chi)\right] + \cos^2 m\phi\,[J_m(\chi) - J_{m+2}(\chi)]\left[k_{mn}J_{m+1}(\chi) - \frac{mJ_m(\chi)}{r}\right]\right\} \tag{5}$$

$$\bar{F}_\phi = -\frac{\partial\bar{U}^{rad}}{r\partial\phi} = \frac{m}{r}\sin 2m\phi\left\{J_m^2(\chi)\left[\frac{f_1}{3}\cos^2\zeta - \frac{f_2}{2}\left(\frac{k_{zl}}{k}\right)^2\sin^2\zeta\right]\zeta + \frac{f_2}{2}\left(\frac{k_{mn}}{k}\right)^2\cos^2\zeta J_{m+1}(\chi)\left[\frac{2mJ_m(\chi)}{\chi} - J_{m+1}(\chi)\right]\right\} \tag{6}$$

$$\bar{F}_z = -\frac{\partial\bar{U}^{rad}}{\partial z} = k_{zl}\sin 2\zeta\left\{J_m^2(\chi)\left[\left(\frac{f_1}{3} + \frac{f_2}{2}\left(\frac{k_{zl}}{k}\right)^2\right)\cos^2 m\phi - \frac{f_2}{2}\left(\frac{m}{kr}\right)^2\right] + \frac{f_2}{2}\left(\frac{k_{mn}}{k}\right)^2 J_{m+1}(\chi)\left[\frac{2mJ_m(\chi)}{\chi} - J_{m+1}(\chi)\right]\cos^2 m\phi\right\} \tag{7}$$

2.3. Numerical model

To reduce computational cost in COMSOL software, we simplify the experimental setup to an axis-symmetrical model, as shown in Fig. 2. For exact modeling of the experimental structure, the cylindrical fluid cavity (white) is modeled by the acoustic pressure module, the silicon wafer (light gray) and reflective layer (dark gray) are modeled by the linear elastic solid module. The piezoelectric plate is PZT-4 actuated in the d33-mode with a driving voltage of 1 V_{pp} at frequency of 4 MHz and 6.28 MHz, which is modeled by coupling stresses and strains with electric field and electric displacement [25]. The acoustic and elastic domain are coupled with pressure and acceleration boundary conditions on the solid-water interface. After obtaining the pressure and velocity field in the cavity, the corresponding ARF acting on a 2.5 μm-radius PS microsphere can be calculated by using Eq. (2) and Eq. (3). The parameters of the materials used are given in Table 1 [25–32].

Table 1
Material properties.

	Density (kg/m^3)	Longitudinal velocity (m/s)	Transverse velocity (m/s)
Saline Water	1050	1490	0
Polystyrene (PS)	1050	2170	1100
Silicon	2329	9660	5340
Glass	2600	5521	3449
Polydimethylsiloxane (PDMS)	965	750	80

Three plates (a glass plate with thickness of 340 μm, a PDMS plate with thickness of 400 μm, and a glass plate with thickness of 660 μm) have been chosen for representation of different kinds of boundary in our experiment. The reasons can be explained as follow. It is well known that soft boundary condition is imposed when the solid medium in contact with the fluid is not able to sustain any pressure, described by the boundary condition $p = 0$, such as free interfaces of water to air. In practice, the deformable elastic materials like PDMS walls might be treated as this soft boundary condition [33]. We choose a PDMS plate with thickness of 400 μm as a soft boundary. A hard boundary condition in an ideal case represents that the interfacing medium does not yield to the velocity of the liquid, i.e., total reflection of the pressure wave ($n\cdot\nabla p = 0$). Fig. 2(b) shows the reflection coefficient of the glass plate at the interface of water and air (incident wave in water) with thickness of 340 μm (black solid line) and 660 μm (red dashed line). It is clearly illustrated that, at the frequency of 4 MHz, the reflection coefficient of the 340 μm-thick glass plate is almost 1, while the reflection coefficient of the 660 μm-thick glass plate is about 0.64. Thus, the former with thickness equal to a quarter wavelength [11] can be represented as a hard boundary condition and the latter can be considered as an imperfect rigid boundary.

3. Results and discussion

3.1. Effects of the rigid top boundary condition

3.1.1. A. Analytical prediction

For this case, the boundary conditions for the cavity can be expressed as: $(\partial p/\partial z)_{z=L} = (\partial p/\partial z)_{z=0} = 0$. Substituting Eq. (1) into these boundary conditions, the wavenumber in the z direction can be obtained as $k_{zl_{\text{rigid}}} = l\pi/L$, $l = 0, 1, 2, \ldots$, while $\varphi_{zl} = 0$. For the frequency 4 MHz, the height $L = 186$μm and radius $a = 419$ μm of the cavity in our experiment are 0.5λ and 1.127λ, respectively. Thus, the cavity in this case can support the (0 2 0) and (0 0 1) eigen modes.

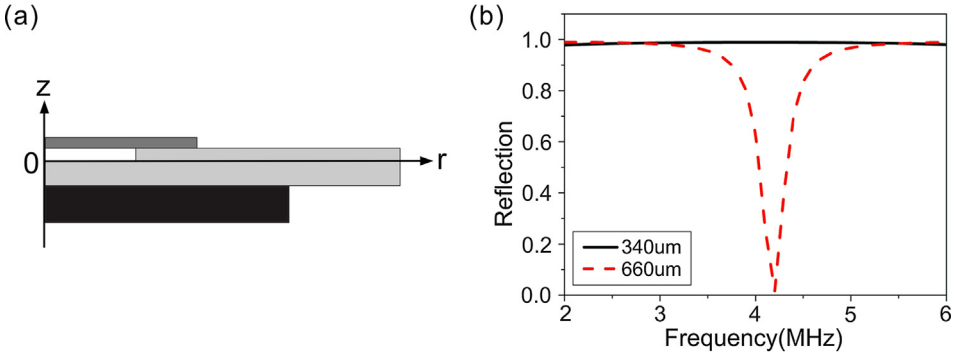

Fig. 2. (a) Model for numerical simulation. It consists of a reflective layer (dark gray), a cylindrical cavity (white) dry-etched in a silicon wafer (light gray) and a piezoelectric plate (black). (b) The reflection of the glass plate with thickness of 340 μm (black solid line) and 660 μm (red dashed line) from water to air.(For interpretation of the references to colour in this figure legend, the reader is referred to the web version of this article.)

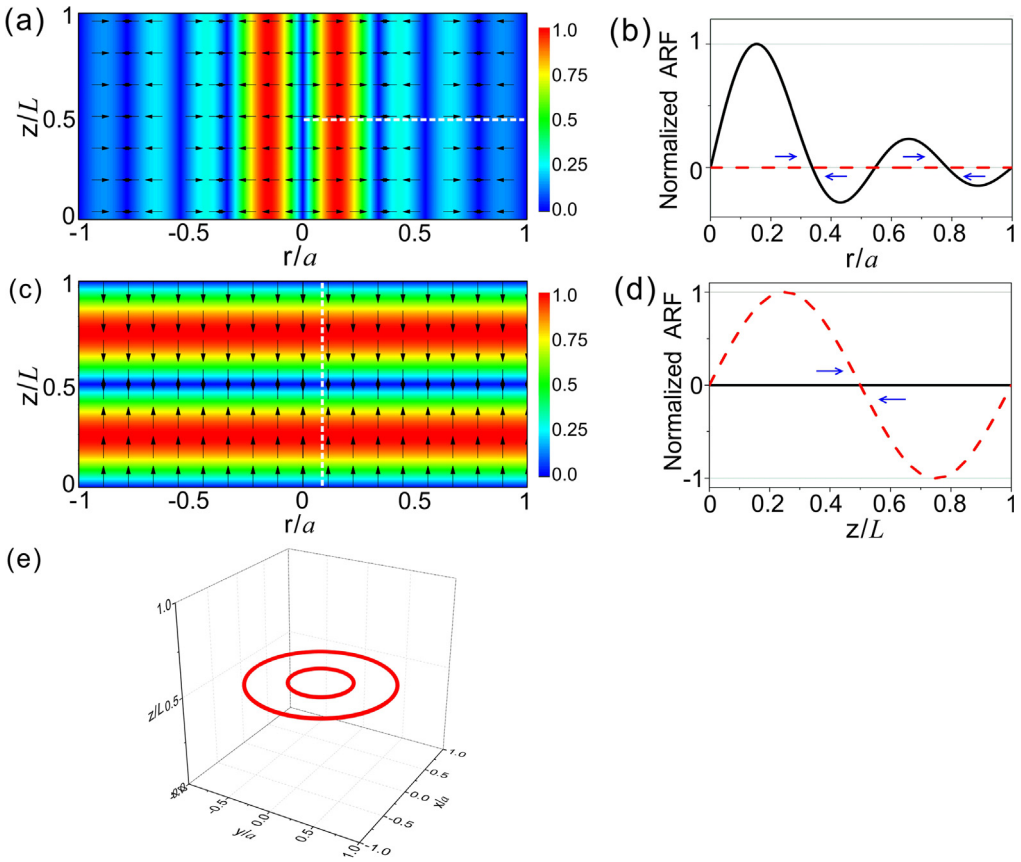

Fig. 3. The normalized ARF distribution of the (0 2 0) eigen mode (a) and the (0 0 1) eigen mode (c) in the rz plane of the cavity with the rigid top boundary condition at the frequency of 4 MHz. (b) and (d) show the F_r (black solid line) and F_z (red dashed line) versus the particle's position at the white dashed line in (a) and (c), respectively. The arrows in (b) and (d) indicate the particle's moving direction by adjacent restoring ARFs. (e) The predicted stable localized positions of the PS particles in the cavity with the rigid top boundary when these two eigen modes are excited simultaneously.(For interpretation of the references to colour in this figure legend, the reader is referred to the web version of this article.)

The amplitude and direction of the dimensionless ARF distribution in the rz plane of the (0 2 0) mode and (0 0 1) mode are shown in Fig. 3a and c, respectively. Fig. 3b and d detailedly illustrate the amplitude of F_r (black solid line) and F_z (red dashed line) versus the position of the white dashed lines in Fig. 3a and c, respectively. For the (0 2 0) mode, the radial force F_r dominates, while F_z are always zero. In addition, there are five critical points ($F_r = 0$) in the radial direction. By analyze the particle's moving direction (blue arrow) according to the direction of the adjacent radial restoring forces, $r = 0.340a$ and $r = 0.786a$ are the stable localized positions [17]. For the (0 0 1) mode, F_z dominates while F_r are always zero. Similarly, there are three critical points ($F_z = 0$) in the z direction and $z = 0.5L$ is the stable localized position.

These two eigen modes can be excited individually when the wave vector of the incident wave perfectly matches with that of the corresponding eigen modes. Nevertheless, for the PZT plate as the actuator in the experiment, the wave vector of the incident wave contains both the radial and z-directional components, resulting in these two modes being excited simultaneously. Thus, the stable positions for these PS particles in the cavity may be the overlapped region of the positions of these two modes, i.e., two circles in the $z = 0.5L$ mid-plane with $r = 0.340a$ and $r = 0.786a$, respectively, as shown in Fig. 3e.

3.1.2. B. Numerical and experimental results

Fig. 4a shows the numerical map of the ARF in the rz plane at the frequency of 4 MHz with the top boundary of the 340 μm-thick glass plate. It is observed that the maximum amplitude of force reaches 8 pN and the stable trapping position ($F = 0$) is a curved line around $z = 0.5L$ in the rz plane. To further recognize the stable position, Fig. 4b illustrates the F_r (black solid line) and F_z (red dashed line) along the white dashed line $z = 0.5L$ in Fig. 4a. The particles are subject to the adjacent radial restoring forces (blue arrow) till they are stably trapped at the equilibrium position at $r = 0.344a$ and $r = 0.751a$ in the $z = 0.5L$ plane.

Fig. 4c–e illustrate the experimental movements of the PS microspheres in the $z = 0.5L$ plane in a time series (see multimedia view 1). It is clearly observed that after the PZT actuated with 83 s, a steady state of PS microspheres can be reached with two circles ($0.359a$, $0.851a$) at $z = 0.5L$, which agrees excellently well with the analytical (Fig. 3e) and numerical predictions (Fig. 4a). Thus, the top boundary of the 340 μm-thick glass plate can be considered as a perfect rigid boundary in this cavity at frequency of 4 MHz.

3.2. Effects of the soft top boundary condition

3.2.1. A. Analytical prediction

If the top wall is a soft surface, the boundary conditions can be expressed as $(\partial p/\partial z)_{z=0} = p_{z=L} = 0$. Substituting Eq. (1) into these boundary conditions, the wavenumber in the z direction can be obtained as $k_{zl_{\text{soft}}} = (l/2 + 0.25)2\pi/L$, $l = 0, 1, 2, \ldots$ while $\varphi_{zl} = 0$. However, at the frequency of 4 MHz, this cavity cannot support any eigen mode. When the frequency changes to 6 MHz, as the corresponding wavelength $\lambda = 248$ μm, the height and radius of the cavity are $L = 0.75\lambda$ and $a = 1.69\lambda$. In this case, the cavity can support the (0 3 0) and (0 0 1) modes.

Fig. 5a and c show the dimensionless ARF distribution in the rz plane of the (0 3 0) and (0 0 1) eigen modes, respectively. For the (0 3 0) mode, both F_r andF_z exist, while for the (0 0 1) mode $F_r = 0$ and F_z dominates. To simplify the analysis, we first plot the normalized r (black solid line) and z components (red dashed line) of the ARF for the

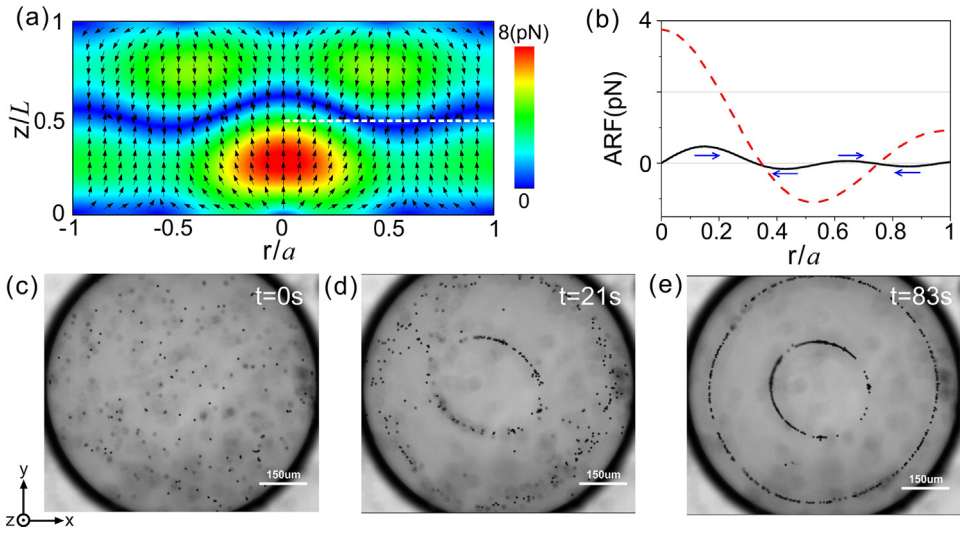

Fig. 4. (a) The numerical map of the total ARF acting on the PS microsphere located in the rz plane of the cylindrical cavity covered with the 340 μm-thick glass plate. (b) The plot of the numerical F_r (black solid line) and F_z (red dashed line) versus the position of particle at the white dashed line $z = 0.5L$ in (a), the arrows indicate the particle's moving direction by adjacent restoring ARFs. (c)–(e) The experimental movements of the PS microspheres in the cavity covered by the 340 μm-thick glass film in the $z = 0.5L$ plane at 4 MHz.(For interpretation of the references to colour in this figure legend, the reader is referred to the web version of this article.)

(0 0 1) mode along the white dashed line $r = 0.1a$ in the rz plane as shown in Fig. 5d. It can be clearly observed that there are four critical points in the z direction and $z = L/3$ is the stable localization position. Thus, for the (0 3 0) mode, we plot two components of the ARF along the white dashed line $z = L/3$ in the rz plane as shown in Fig. 5b. The stable localization positions are indicated as $r = 0.234a$, $r = 0.542a$ and $r = 0.824a$ where both F_r and F_z go to zero, and the blue arrows denote the adjacent radial restoring forces indicating the particle's moving

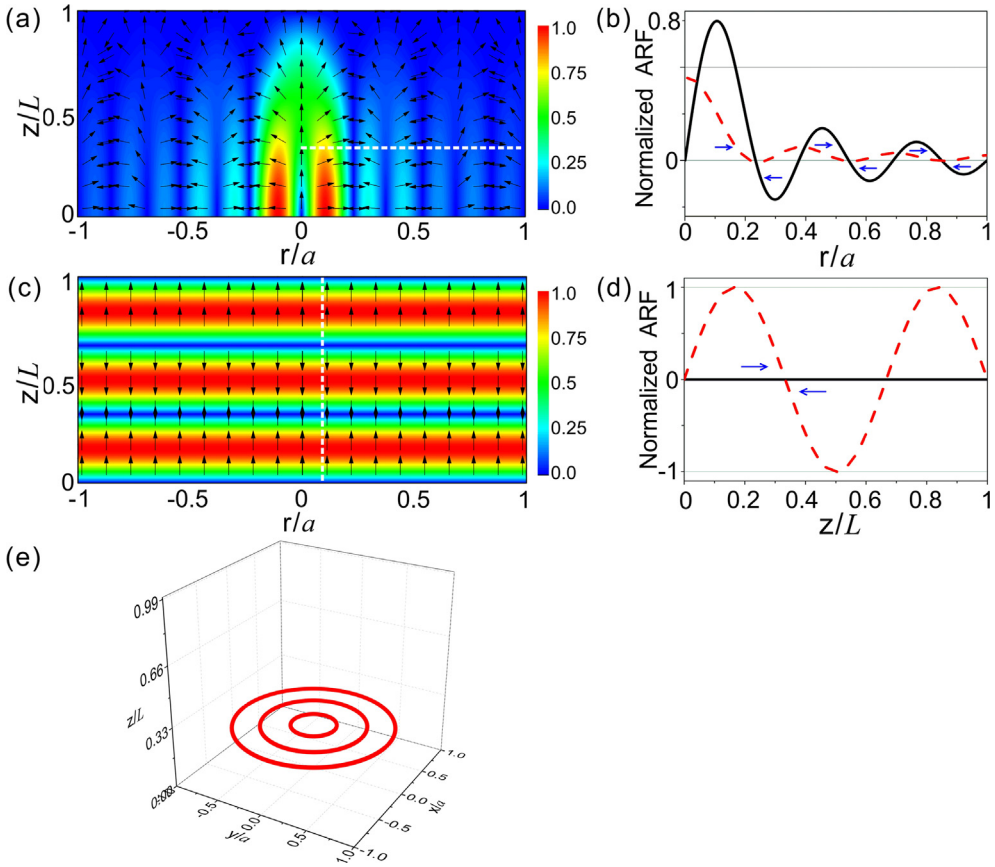

Fig. 5. The normalized ARF distribution of the (0 3 0) eigen mode (a) and the (0 0 1) eigen mode (c) in the rz plane of the cavity with the soft top boundary condition at the frequency of 6 MHz. (b) and (d) show the F_r (black solid line) and F_z (red dashed line) versus the particle's position at the white dashed line in (a) and (c), respectively. The arrows in (b) and (d) indicate the particle's moving direction by adjacent restoring ARFs. (e) The predicted stable localized positions of the PS particles in the cavity with the soft top boundary when these two eigen modes are excited simultaneously.(For interpretation of the references to colour in this figure legend, the reader is referred to the web version of this article.)

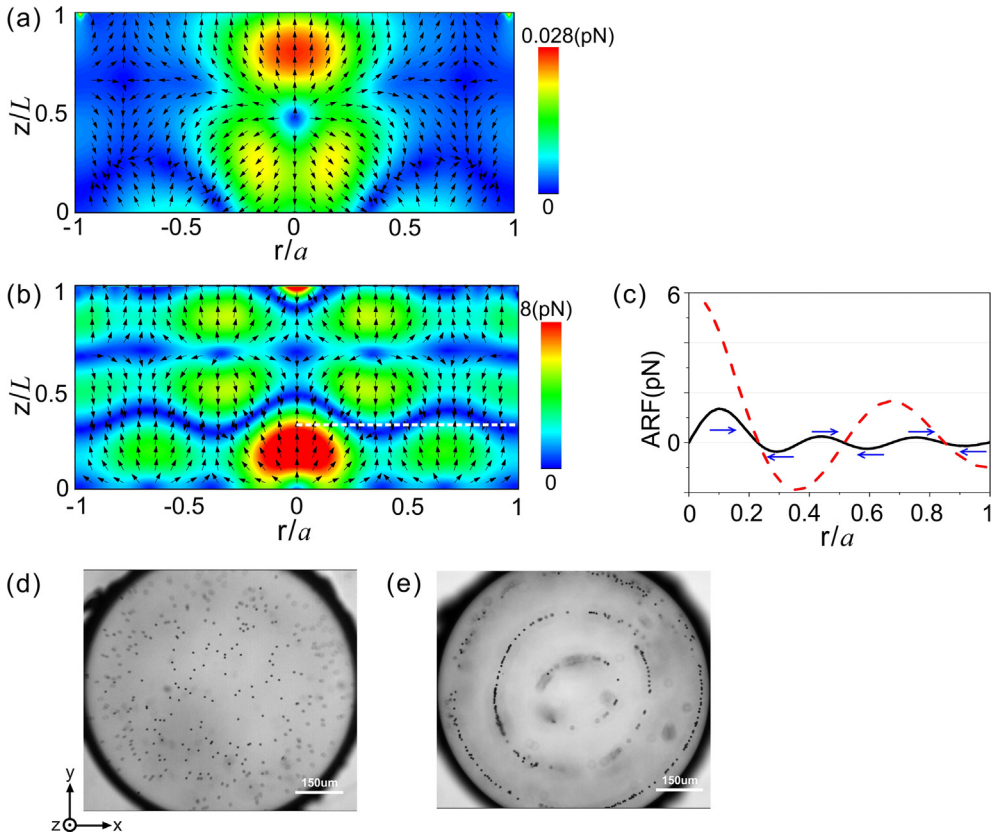

Fig. 6. The numerical map of the total ARF acting on a PS microsphere in the rz plane of the cylindrical cavity covered with the 400 μm-thick PDMS plate at the frequency of 4 MHz (a) and 6.28 MHz (b). (c) The plot of the numerical F_r (black solid line) and F_z (red dashed line) versus the position of particle at the white dashed line $z = L/3$ in (b), the arrows indicate the particle's moving direction by adjacent restoring ARFs. The experimental movements of the PS microspheres in the cavity covered by the 400 μm-thick PDMS plate at frequency of 4 MHz (d) and 6.28 MHz (e) in the $z = L/3$ plane.(For interpretation of the references to colour in this figure legend, the reader is referred to the web version of this article.)

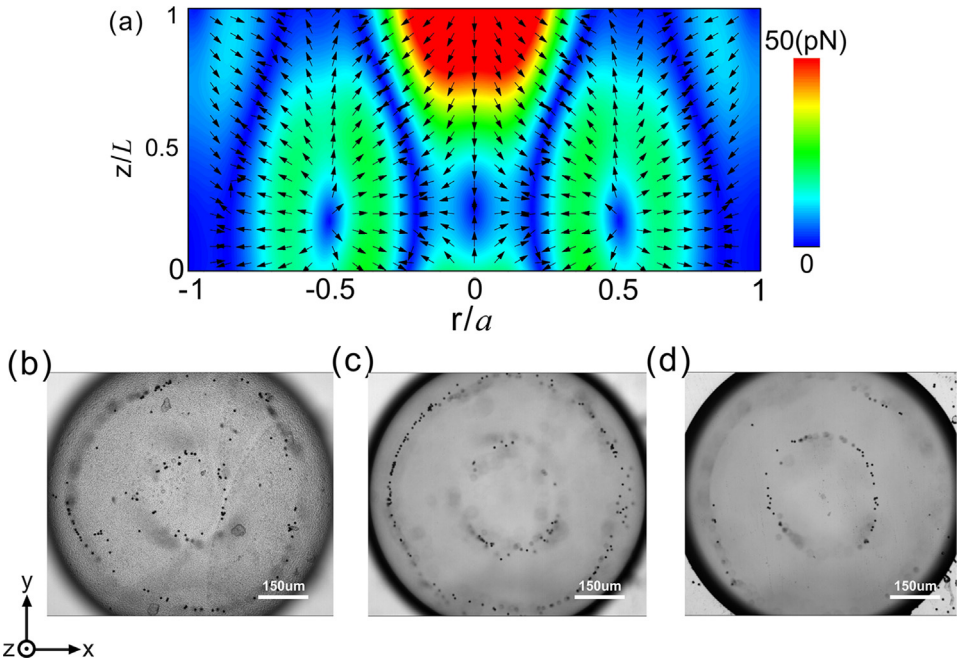

Fig. 7. (a) The numerical map of the total ARF acting on a PS microsphere located in the rz plane of the cavity covered by the 660 μm-thick glass plate representing the imperfect rigid boundary. The experimental status of the PS microspheres in the plane of $z = 0$ (b), $z = 0.5L$ (c), and $z = L$ (d) after the PZT actuated with 78 s. (For interpretation of the references to colour in this figure legend, the reader is referred to the web version of this article.)

direction. Similarly, for the PZT plate as the actuator, these two modes are excited simultaneously, thus the stable positions of PS particles in the cavity could be three circles located at $r = 0.234a$, $r = 0.542a$, $r = 0.824a$ in the $z = L/3$ plane as shown in Fig. 5e.

3.2.2. B. Numerical and experimental results

We first numerically investigate the ARF acting on the PS microsphere in the rz plane of the cavity covered with the 400 μm-thick PDMS plate at the frequency of 4 MHz, as shown in Fig. 6a. It is observed that the maximum magnitude of the ARF is just about 0.028 pN which is much smaller than that of the rigid top boundary condition with 8 pN. Thus, PS microspheres may not have stable positions in this case. Then, we depict the corresponding ARF distribution acting on the PS microsphere at the frequency of 6.28 MHz in Fig. 6b, and the detailed F_r and F_z along the white dashed line $z = L/3$ in Fig. 6c. The maximum force is about 8 pN, which is two orders of magnitude larger than that at 4 MHz. Besides, the forces are equal to zero at these three circles of $r = 0.227a$, $0.515a$ and $0.846a$ in the $z = L/3$ plane. PS microspheres may be stably localized at these positions.

In the experiment, we also first observe the movements of the PS microspheres in the cavity covered with the 400-μm-thick PDMS plate at the frequency of 4 MHz. As shown in Fig. 6d and multimedia view 2, the particles move very slowly and cannot be stably trapped. Then the frequency is switched to 6.28 MHz, these PS microspheres can be trapped in three circles ($0.262a$, $0.593a$, $0.909a$) at the $z = L/3$ plane after about 50 s (Fig. 6e and multimedia view 2). On the whole, the stable positions in the experiment coincide with that of theoretical predictions, expect that some particles of the first inner circle are slightly off the $z = L/3$ stable plane. This can be attributed to the fact that the PDMS plate cannot be considered as a perfect soft boundary.

3.3. Effects of the imperfect rigid top boundary condition

For the case of the cavity covered with the imperfect rigid boundary, it is difficult to analytically analyze the eigen modes and corresponding ARFs. Thus, we just investigate this case numerically and experimentally. Fig. 7a illustrates the numerical map of the ARF acting on a PS microsphere in the rz plane at the frequency of 4 MHz, while the top boundary is the 660 μm-thick glass plate representing the imperfect rigid boundary. The maximum amplitude of force is about 50 pN which is comparable to that of the rigid boundary. In addition, there are four force minima planes in the radial direction and no stable trapping plane in the z direction. This is similar to the analytical solution of the eigen mode (0 2 0) under the rigid top boundary (Fig. 3a) that the radial force dominates. Thus, particles may be formed two circles at multiple planes from $z = 0$ to $z = L$ throughout the cavity.

The experimental status of these PS microspheres in the cavity covered by the 660 μm-thick glass plate are shown in Fig. 7b–d at the plane of $z = 0$, $z = 0.5L$ and $z = L$, respectively. As expected, PS microspheres can be reached with two circles at multiple planes (multimedia view 3). In addition, the first inner circle of the stable position becomes larger as the position in the z direction gets higher. This phenomenon agrees well with the numerical simulations.

4. Conclusions

We analytically, numerically and experimentally investigate the effects of boundary conditions on acoustic manipulation of particles in a cylindrical microfluidic cavity. The boundary conditions greatly influence on the eigen mode excitation of the cavity, as well as the ARF distribution and the particles' stable positions. The total reflective plate with thickness equal to a quarter wavelength can be considered as the rigid boundary, while the PDMS plate and the partly reflective plate can be regarded as the soft and imperfect rigid boundary. These experimental phenomena are in good agreement with the analytical and numerical predictions. The present investigation demonstrates that the effects of boundary conditions need to be considered for precise acoustic manipulation.

Acknowledgements

The work was supported by the National Key Research and Development Program of China (Grant No. 2016YFA0201001), the 973 Program (Grant No. 2015CB755500), and the National Natural Science Foundation of China (Grant Nos. 11674346, 11674347, 11404363, 11534013, 81527901, 11774369). F. Cai's work was partially supported by the Shenzhen Basic Research Program (Grant No. JCYJ20170818163258397) and the Scientific Instrument Innovation Team of Chinese Academy of Sciences, GJJSTD20180002. L. Meng's work was partially supported by the Shenzhen Basic Research Program (No. JCYJ20160429184552717) and the Key Laboratory for Magnetic Resonance and Multimodality Imaging of Guangdong Province(No. 2014B030301013).

Appendix A. Supplementary material

Supplementary data to this article can be found online at https://doi.org/10.1016/j.ultras.2018.10.003.

References

[1] F. Guo, P. Li, J.B. French, Z. Mao, H. Zhao, S. Li, N. Nama, J.R. Fick, S.J. Benkovic, T.J. Huang, Controlling cell-cell interactions using surface acoustic waves, PNAS 112 (1) (2015) 43–48.
[2] A.L. Bernassau, P. Glynne-Jones, F. Gesellchen, M. Riehle, M. Hill, D.R.S. Cumming, Controlling acoustic streaming in an ultrasonic heptagonal tweezers with application to cell manipulation, Ultrasonics 54 (2014) 268–274.
[3] T. Laurell, F. Petersson, A. Nilsson, Chip integrated strategies for acoustic separation and manipulation of cells and particles, Chem. Soc. Rev. 36 (3) (2007) 492–506.
[4] B. Hammarström, M. Evander, H. Barbeau, M. Bruzelius, J. Larsson, T. Laurell, J. Nilsson, Non-contact acoustic cell trapping in disposable glass capillaries, Lab Chip 10 (2010) 2251–2257.
[5] M. Antfolk, C. Magnusson, P. Augustsson, H. Lilja, T. Laurell, Acoustofluidic, label-free enrichment and simultaneous concentration of rare tumor cells from white blood cells, Anal. Chem. 87 (2015) 9322–9328.
[6] L. Meng, F. Cai, Z. Zhang, L. Niu, Q. Jin, F. Yan, J. Wu, Z. Wang, H. Zheng, Transportation of single cell and microbubbles by phase-shift introduced to standing leaky surface acoustic waves, Biomicrofluidics 5 (4) (2011) 044104–044110.
[7] O. Manneberg, B. Vanherberghen, B. Onfelt, M. Wiklund, Flow-free transport of cells in microchannels by frequency-modulated ultrasound, Lab Chip 9 (6) (2009) 833–837.
[8] X. Ding, S.-C.S. Lin, B. Kiraly, H. Yue, S. Li, I.-K. Chiang, J. Shi, S.J. Benkovic, T.J. Huang, On-chip manipulation of single microparticles, cells, and organisms using surface acoustic waves, PNAS 109 (28) (2012) 11105–11109.
[9] G. Kaduchak, D.N. Sinha, D.C. Lizon, Novel cylindrical, air-coupled levitation/concentration device, Rev. Sci. Instrum. 73 (2002) 1332–1336.
[10] A. Neild, S. Oberti, J. Dual, Design, modeling, and characterization of microfluidic devices for ultrasonic manipulation, Sens. Actuat. B 121 (2007) 452–461.
[11] A. Lenshof, M. Evander, T. Laurell, J. Nilsson, Acoustofluidics 5: building microfluidic acoustic resonators, Lab Chip 12 (2012) 684–695.
[12] M.-S. Scholz, B.W. Drinkwater, R.S. Trask, Ultrasonic assembly of anisotropic short fibre reinforced composites, Ultrasonics 54 (2014) 1015–1019.
[13] S. Yamahira, S. Hatanaka, M. Kuwabara, S. Asai, Orientation of fibers in liquid by ultrasonic standing waves, Jpn. J. Appl. Phys. 39 (2000) 3683–3687.
[14] W. Wang, L.A. Castro, M. Hoyos, T.E. Mallouk, Autonomous motion of metallic micro-rods propelled by ultrasound, ACS Nano 6 (2012) 6122–6132.
[15] B. Raeymaekers, C. Pantea, D.N. Sinha, Manipulation of diamond nanoparticles using bulk acoustic waves, J. Appl. Phys 109 (1) (2011) 014317.
[16] P. Augustsson, T. Laurell, Acoustofluidics 11: affinity specific extraction and sample decomplexing using continuous flow acoustophoresis, Lab Chip 12 (2012) 1742.
[17] M. Barmatz, P. Collas, Acoustic radiation potential on a sphere in plane, cylindrical, and spherical standing wave fields, J. Acoust. Soc. Am. 77 (3) (1985) 928–945.
[18] M. Barmatz, P. Collas, Erratum: Acoustic radiation potential on a sphere in plane, cylindrical, and spherical standing waves [J. Acoust. Soc. Am. 77 (3), 928–945 (1985)], J. Acoust. Soc. Am. 140 (2016) 3519.
[19] J. Wang, J. Dual, Theoretical and numerical calculation of the acoustic radiation force acting on a circular rigid cylinder near a flat wall in a standing wave excitation in an ideal fluid, Ultrasonics 52 (2012) 325–332.
[20] R. Yamamoto, D. Koyama, M. Matsukawa, On-chip ultrasonic manipulation of microparticles by using the flexural vibration of a glass substrate, Ultrasonics 79 (2017) 81–86.
[21] P.B. Muller, M. Rossi, Á.G. Marín, R. Barnkob, P. Augustsson, T. Laurell, C.J. Kähler,

H. Bruus, Ultrasound-induced acoustophoretic motion of microparticles in three dimensions, Phys. Rev. E. 88 (2013) 2.
[22] L.E. Kinsler, A.R. Frey, A.B. Coppens, J.V. Sanders, Fundamentals of Acoustics, John Wiley & Sons, Inc., 1999.
[23] H. Bruus, Acoustofluidics 2: perturbation theory and ultrasound resonance modes, Lab Chip 12 (1) (2012) 20–28.
[24] L.P. Gor'kov, On the forces acting on a small particle in an acoustical field in an ideal fluid, Sov. Phys. Dokl. 6 (1962) 773.
[25] http://www.comsol.com/.
[26] D. Fuard, T. Tzvetkova-Chevolleau, S. Decossas, P. Tracqui, P. Schiavone, Optimization of poly-di-methyl-siloxane (PDMS) substrates for studying cellular adhesion and motility, Microelectron. Eng. 85 (2008) 1289–1293.
[27] D. Rabaud, P. Thibault, M. Mathieu, P. Marmottant, Acoustically bound microfluidic bubble crystals, Phys. Rev. L. 106 (2011) 134501.
[28] Z. Mao, Y. Xie, F. Guo, L. Ren, P. Huang, Y. Chen, J. Rufo, F. Costanzoa, T.J. Huang, Experimental and numerical studies on standing surface acoustic wave microfluidics, Lab Chip 16 (2016) 515–524.
[29] L. Johansson, J. Enlund, S. Johansson, I. Katardjiev, V. Yantchev, Surface acoustic wave induced particle manipulation in a PDMS channel—principle concepts for continuous flow applications, Biomed. Microdevices 14 (2) (2012) 279–289.
[30] E. Madsen, H. Sathoff, J. Zagzebski, Ultrasonic shear wave properties of soft tissues and tissuelike materials, J. Acoust. Soc. Am. 74 (5) (1983) 1346–1355.
[31] J. Tsou, J. Liu, A. Barakat, M. Insana, Role of ultrasonic shear rate estimation errors in assessing inflammatory response and vascular risk, Ultrasound Med. Biol. 34 (6) (2008) 963–972.
[32] B.E. Treeby, B.T. Cox, Modeling power law absorption and dispersion in viscoelastic solids using a split-field and the fractional Laplacian, J. Acoust. Soc. Am. 136 (4) (2014) 1499–1510.
[33] N. Bose, X. Zhang, T.K. Maiti, S. Chakraborty, The role of acoustofluidics in targeted drug delivery, Biomicrofluidics 9 (2015) 052609.